Nuclear Instruments and Methods in Physics Research A 784 (2015) 80–87

Contents lists available at ScienceDirect

Nuclear Instruments and Methods in Physics Research A

journal homepage: www.elsevier.com/locate/nima

Comparing the response of PSD-capable plastic scintillator to standard liquid scintillator

Richard S. Woolf [a,*], Anthony L. Hutcheson [a], Chul Gwon [a], Bernard F. Phlips [a], Eric A. Wulf [a]

[a] High Energy Space Environment Branch, Space Science Division, U. S. Naval Research Laboratory, 4555 Overlook Ave., SW, Washington, DC 20375

ARTICLE INFO

Available online 6 November 2014

Keywords:
Pulse shape discrimination
Plastic scintillator
Liquid scintillator
EJ-299-33
EJ-301
EJ-309

ABSTRACT

This work discusses a test campaign to characterize the response of the recently developed plastic scintillator with pulse shape discrimination (PSD) capabilities (EJ-299-33). PSD is a property exhibited by certain types of scintillating material in which incident stimuli (fast neutrons or γ rays) can be separated by exploiting differences in the scintillation light pulse tail. Detector geometries used were: a 10 cm × 10 cm × 10 cm cube and a 10-cm diameter × 10-cm long cylinder. EJ-301 and EJ-309 liquid scintillators with well-known responses were also tested. The work was conducted at the University of Massachusetts Lowell Van De Graaff accelerator. The facility accelerated protons on a thin Li target to yield quasi-monoenergetic neutrons from the ^{7}Li(p,n)^{7}Be reaction (Q-value: –1.644 MeV). Collimated fast neutrons were obtained by placing detectors behind a neutron spectrometer. Rotating the spectrometer, and thus changing the neutron energy, allowed us to achieve 0.5–3.2 MeV neutrons in 200–300 keV steps. Data were acquired through a flash analog-to-digital converter (ADC) capable of performing digital PSD measurements. By using the PSD technique to separate the neutron events from unwanted γ background, we constructed a pulse height spectrum at each energy.

Obtaining a relationship of the relative light output versus energy allowed us to construct the response function for the EJ-299-33 and liquid scintillator. The EJ-299-33 response in terms of electron equivalent energy ($E_{e.e.}$) vs. proton equivalent energy ($E_{p.e.}$), how it compared with the standard xylene-based EJ-301 (or, NE-213/BC-501 A equivalent) and EJ-309 liquid scintillator response, and how the EJ-301 and EJ-309 compared, are presented. We find that the EJ-299-33 demonstrated a lower light output by up to 40% for $<$ 1.0 MeV neutrons; and ranging between a 5–35% reduction for 2.5–3.0 MeV neutrons compared to the EJ-301/309, depending on the scintillator and geometry. Monte Carlo modeling techniques were used to investigate how the neutron beam and accelerator background environment affected the detector response. We find relatively good agreement between our results and the modeling; however, the observed response could not be fully accounted for due to events with pulse pile up, thus leading to contamination of the neutron PSD selected events.

Published by Elsevier B.V.

1. Introduction

Until recently, the ability to perform pulse shape discrimination (PSD) – a property exhibited by certain types of scintillating material in which incident (n/γ) stimuli can be separated by exploiting differences in the tail of their light pulses – in plastic scintillator was difficult, if not impossible [1]. A newly developed plastic scintillator capable of PSD [2] is now commercially available through Eljen Technology (EJ-299-33) [3]. Prior to this advent, only certain liquid and organic crystal scintillators (e.g., stilbene, anthracene, p-terphenyl) could perform PSD. Separating fast neutrons from the γ-ray background and performing neutron spectroscopy are important for applications in neutron physics, such as experimental nuclear physics [4], homeland defense [5], and near-Sun observing spacecraft [6]. Using plastic scintillators for said applications, as opposed to the commonly used aforementioned PSD-capable materials, has been desired in the field on neutron physics for the last half century. The downfalls of liquid scintillators are that the material is caustic, flammable, and toxic, raising concern for field-deployable systems and spacecraft; organic scintillating crystals are typically more costly than plastics and more difficult to grow to a large size. An understanding of the scintillation light response function is paramount to the full characterization of this novel detector.

* Corresponding author. Tel.: +1 (202) 404 2886; fax: +1 (202) 767 6473.
E-mail addresses: richard.woolf@nrl.navy.mil (R.S. Woolf), anthony.hutcheson@nrl.navy.mil (A.L. Hutcheson), chul.gwon@nrl.navy.mil (C. Gwon), bernard.phlips@nrl.navy.mil (B.F. Phlips), eric.wulf@nrl.navy.mil (E.A. Wulf).

http://dx.doi.org/10.1016/j.nima.2014.10.067
0168-9002/Published by Elsevier B.V.

This work discusses a campaign that was carried out in December of 2013 to characterize the EJ-299-33 response, complementing work done by others in the community [7–10]. The main goal of this work was to understand the relationship between the amount of scintillation light yielded by fast neutrons interacting with constituent hydrogen nuclei, producing energetic recoil protons in the process. The way to properly investigate this relationship is to characterize the detector response as a function of incident neutron energy. To produce single-energy neutron emission, one must accelerate charged particles and allow them to undergo subsequent nuclear reactions, resulting in quasi-monoenergetic neutrons. By characterizing a PSD-capable radiation detector with quasi-monoenergetic neutrons, along with γ rays (to relate scintillator light output and recoil electron energy from interactions with atomic electrons), one can obtain a relationship between the neutron light output (charge collected over some integration time) and the neutron energy deposit. The common avenue to obtain a tunable source of quasi-monoenergetic neutron emission is at an accelerator facility, such as a cyclotron [11] or a Van de Graaff [12]. One can also obtain single-energy neutron emission through compact neutron generators that employ fusion reactions, such as deuterium–deuterium (*D–D* releasing $E_n = 2.4$ MeV) or deuterium–tritium (*D–T* releasing $E_n = 14.1$ MeV) [13].

To better understand the resultant distribution in energy obtained from a measurement with a radiation detector, a simulation of the experiment can be conducted through Monte Carlo modeling techniques. Modeling allows the user to define the details of the experiment (detector setup, spectrum, environment, etc.) and, based on first principles, numerically step through and track each particle, determining the interaction process and energy deposited along the way. By creating an ensemble of these events and applying specific detector resolution ($\delta E/E$) functions, one can obtain results that can then be compared to the empirical data.

2. Experimental method

Detector characterization was conducted using the 5.5 MV Van de Graaff accelerator located at the University of Massachusetts Lowell (UML) [14] (Fig. 1). The accelerator produces energetic protons that are directed onto a thin (10 μm) Li target, resulting in quasi-monoenergetic neutrons from the ^{7}Li(p,n)^{7}Be reaction. Typical accelerator current ranged between 1 and 5 μA. The energy spread due to dE/dx losses in the target is of order 50 keV. The reaction is endothermic with a Q-value of −1.644 MeV; thus, the energy of the outgoing neutron is the difference between the proton beam energy and the Q-value. Secondary reactions result from the first excited state of ^{7}Be, i.e., ^{7}Li(p,n)^{7}Be*; the Q-value for this reaction is −2.075 MeV. At a fixed proton beam energy, different neutron energies are obtained by rotating a neutron spectrometer between 0° (on axis) to points off axis up to 135° – the maximum allowed backward angle. The spectrometer consists of a paraffin and Li_2CO_3 collimator [15] located 2.6 m from the target.

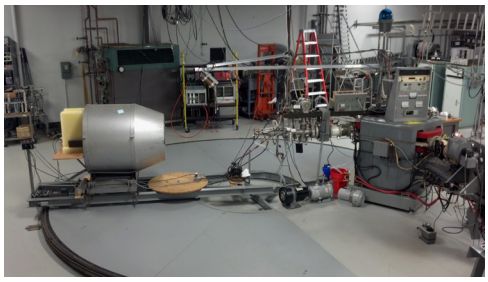

Fig. 1. Experimental setup at the University of Massachusetts Lowell Van De Graaff accelerator. Shown on the left is the neutron spectrometer, behind which the detector and paraffin wax shielding were placed.

The accelerator nominally ran with proton beam energies of 3.0 and 4.0 MeV. Tables 1 and 2 show the angle of the neutron spectrometer with respect to the beam and the resulting neutron energies obtained for 3.0 and 4.0 MeV, respectively. The angle of the spectrometer with respect to the beam was determined by markings on the rail along which the spectrometer rotated. There is an offset of 0.06 m between the location of the Li target and the axis of rotation. The angles listed in Tables 1 and 2 were corrected for the offset. The angle-dependent neutron energy was determined by previous work done on the angular distribution of the ^{7}Li(p,n)^{7}Be reaction in the laboratory system [16]. A set of Legendre functions were fit to these data to derive a functional form for the energy-angle relationship (Fig. 2). The fourth-order Legendre polynomial that provided the best fit to the empirical

Table 1
Angular dependency of the ground and first excited state neutron energy for a 3.0 MeV proton beam.

Corrected angle (degrees)	Ground state neutron energy (MeV)	First excited state neutron energy (MeV)
0°	1.306 MeV	0.827 MeV
43.9°	1.144 MeV	0.686 MeV
74.5°	0.920 MeV	0.512 MeV
88.4°	0.819 MeV	0.431 MeV
133.9°	0.579 MeV	0.271 MeV

Table 2
Angular dependency of the ground and first excited state neutron energy for a 4.0 MeV proton beam.

Corrected angle (degrees)	Ground state neutron energy (MeV)	First excited state neutron energy (MeV)
0°	2.323 MeV	1.87 MeV
43.9°	2.079 MeV	1.65 MeV
74.5°	1.734 MeV	1.33 MeV
88.4°	1.574 MeV	1.2 MeV
111.1°	1.348 MeV	1.0 MeV
133.9°	1.179 MeV	0.86 MeV

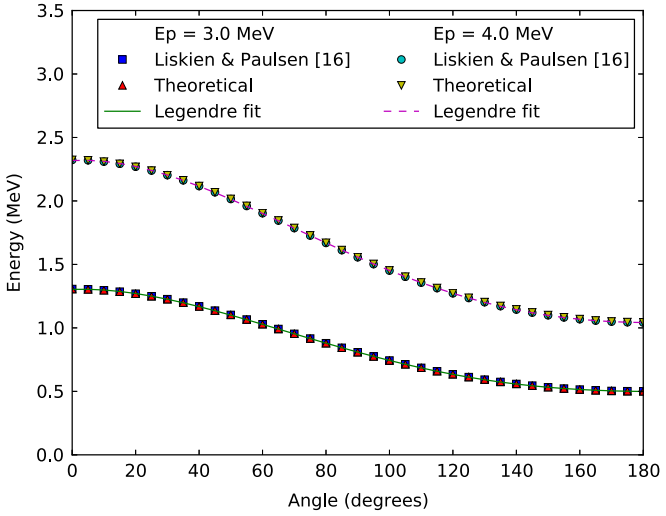

Fig. 2. Neutron energy-angle relationship in the laboratory system for the ^{7}Li(p,n)^{7}Be reaction for a 3.0 and 4.0 MeV proton beams. Empirical data from [16] were fit with a 4th order Legendre polynomial to derive a functional relationship.

data is given in Eq. (1):

$$E = aP_0 + bP_1 + cP_2 + dP_3 + eP_4 \quad (1)$$

where P_n ($n=0$, …, 4) are the Legendre polynomials and the coefficients are: $a=1.3$, $b=8.1\ e^{-4}$, $c=-9.3\ e^{-5}$, $d=3.7\ e^{-7}$, $e=-4.1\ e^{-10}$ for a 3.0 MeV proton beam and $a=2.3$, $b=1.3\ e^{-3}$, $c=-1.4\ e^{-4}$, $d=5.4\ e^{-7}$, $e=-5.5\ e^{-10}$ for a 4.0 MeV proton beam. As shown in Fig. 2, rotation angles $<45^\circ$ result in a small change in the neutron energy; thus, angles between 0° and 43.9° (accounting for the aforementioned offset) were not used. The spectrometer was stepped in the increments shown in Tables 1 and 2 to obtain a range of neutron energies in approximately 200–300 keV steps. Following the range of angles at 3.0 and 4.0 MeV, the neutron spectrometer remained on axis, and the Van de Graaff accelerator was operated at 4.2, 4.5, 4.7, and 4.9 MeV, resulting in neutron energies of 2.52, 2.82, 3.03, and 3.23 MeV, respectively. Varying the proton beam energy and the angle of the spectrometer allowed for the range of neutron energies between 0.5–3.2 MeV. The energy spread resulting from the angular acceptance of the spectrometer is of order 1%.

3. Equipment

3.1. Detectors

We tested two PSD-capable plastic scintillation (EJ-299-33) detectors of different geometries: 10 cm × 10 cm × 10 cm cube and 10-cm diameter × 10-cm long cylinder. Our group at NRL received the bare scintillator from Eljen Technology then assembled a radiation detection instrument. The plastic was wrapped with a thin, white diffuse reflective material, followed by a layer of pliable black cardboard paper. A 78-mm diameter hole was cut into the wrapping to match the diameter of the Electron Tubes Limited (ETL) [17] photomultiplier tube (PMT): ETL 9265KB (14-pin, nine-dynode stage PMT). The PMT was epoxied (manufactured by EPO-TEK) onto the scintillator surface and allowed to cure for a period of 24 h. The outer layer of material and PMT were then wrapped with several layers of black electrical tape.

For comparison studies, we tested liquid scintillation detectors with well-known response functions: the xylene-based EJ-301 [18], or NE-213 equivalent, (12.7-cm diameter × 12.7-cm long cylinder) and EJ-309 [19] (10 cm × 10 cm × 10 cm and 15 cm × 15 cm × 15 cm cubes). EJ-309 is comparable to EJ-301 in terms of response and light output, albeit with a higher flash point temperature. Table 3 lists the salient properties of each scintillator tested. The liquid scintillation detectors were fabricated by SCIONIX Holland B.V. The EJ-301 liquid is housed in 2-mm thick aluminum with a light-tight fixture for the 130-mm Photonis XP4572B PMT (20 pin, 10 dynode stages). The EJ-309 liquid-based detectors were manufactured in the same manner. The 10 cm × 10 cm × 10 cm EJ-309 cube used the 78-mm ETL 9821 PMT (20 pin, 12 dynode stages); the 15 cm × 15 cm × 15 cm EJ-309 cube used the 130-mm ETL 9390 (14 pin, 10 dynode stages).

At the UML facility, detectors were placed directly behind the opening (⌀ 15 cm) of the neutron spectrometer (Fig. 3). To reduce the fast neutron background and the number of down-scattered neutrons, all exposed sides of the detector were shielded with 12-cm thick paraffin wax.

Table 3
Salient properties of the organic scintillating material used in the UML test campaign.

	EJ-299-33	EJ-301	EJ-309
Light output, % Anthracene	56	78	75
photoelectrons/1 MeV e-	8,600	12,000	11,500
Hydrogen-to-Carbon ratio	1.06	1.21	1.25
Density, g/cc	1.08	0.874	0.964

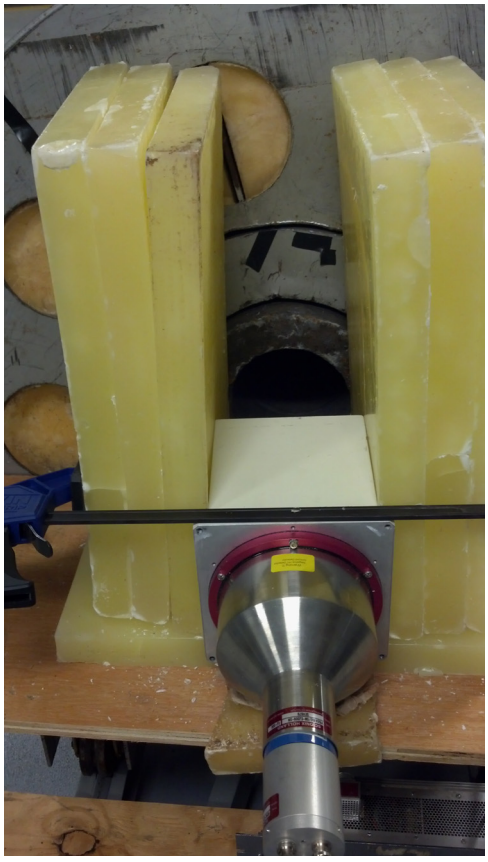

Fig. 3. Liquid scintillator detector located behind the neutron spectrometer exit. All detectors were shielded with 12-cm-thick paraffin wax to reduce the down-scattered neutron background (the top was unshielded for the purpose of the photograph only).

3.2. Electronics

The high voltage was supplied to each detector by either a 32-channel, ISEG high voltage module (maximum output voltage: ±3 kV; current: 500 μA) [20] or a CAEN SY2527 power supply system with a 12-channel negative high voltage board (maximum output voltage: – 6 kV; current: 1 mA) [21]. The EJ-299-33 detectors were operated with positive biases of 990 V (cube) and 1000 V (cylinder). The 15 cm × 15 cm × 15 cm EJ-309 cube was operated at a negative bias of 830 V. The 20-pin PMT output on the 10 cm × 10 cm × 10 cm EJ-309 cube and 12.7-cm diameter EJ-301 detectors required a higher bias (and thus higher current) to yield comparable gains to the EJ-299-33 detectors and 15 cm × 15 × cm × 15 cm EJ-309 cube. The high voltage was provided by the CAEN supply with negative biases of 1900 V (EJ-309) and 1580 V (EJ-301), each drawing in the range of 800–900 μA. Data were acquired by a 16-channel, 250- MHz Struck Innovative Systeme VME flash digitizing ADC (SIS3316) [22], capable of performing digital PSD measurement. The input to each SIS3316 channel is a negative, fast-rise signal, read in from the detector by a 40′ BNC cable.

3.2.1. Digital PSD

The acquisition system performed digital PSD through the charge integration method [23] where the charge pulse was integrated over user-defined gate widths – a *short* gate (on the order of 50 *ns*) and a *long* gate (on the order of 500 *ns*) – and the

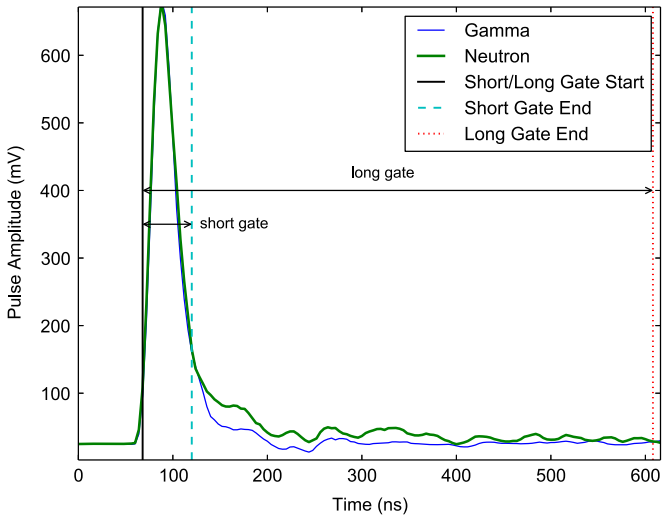

Fig. 4. Representative pulse shape for a γ-ray and neutron (bold curve) induced event in the EJ-299-33 plastic scintillator. The vertical line prior to the peak of the pulse indicates the start of the integration gate window; the subsequent vertical lines indicate the region of the pulse over which the *short* and *long* gates were integrated.

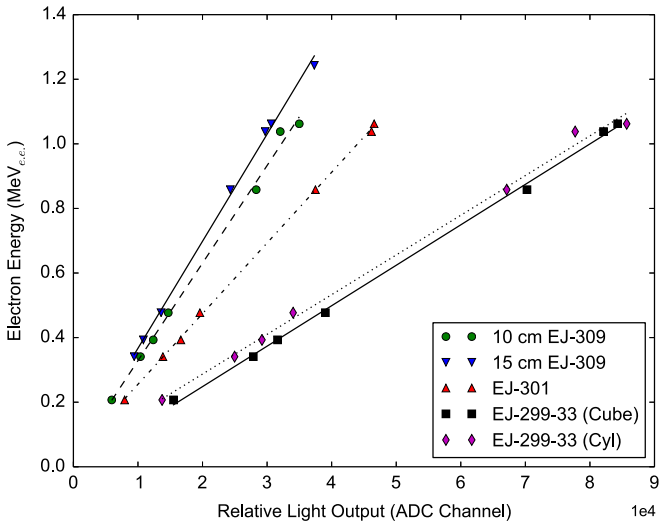

Fig. 5. Calibration curves, expressed in terms of the electron equivalent energy ($MeV_{e.e.}$) vs. the relative light output (ADC channel), for each detector used during the experiment at UML.

ratio of each gate was compared to reveal differences in the decay of the tail pulse arising from different scintillation mechanisms dependent on the incident stimuli. The pulse shape parameter used is $1 - Q_S/Q_L$, where Q_S (Q_L) is the short (long) charge integration gate window. Fig. 4 shows a representative pulse (rendered using a 5-point running boxcar average) arising from either an incident γ ray or neutron (*bold curve*); the vertical lines indicate the regions that define the *short* and *long* integration gates.

4. Results

4.1. Calibration and initial neutron beam measurements

Various radioactive laboratory check sources (^{241}Am, ^{57}Co, ^{133}Ba, ^{137}Cs, ^{207}Bi, ^{60}Co, and ^{22}Na) were used to calibrate each detector response to monoenergetic γ rays, obtaining a relationship between the light output response in terms of electron equivalent energy ($E_{e.e.}$). As expected from previous work, the detector light output is linear for increasing $E_{e.e.}$ (Fig. 5). The maximum Compton recoil electron energy is found at 0.89 ± 0.07 the maximum height of the Compton edge [24]. The minimum detectable threshold for each detector, in terms of $E_{e.e.}$, was: EJ-299-33 (cube): ~30 $keV_{e.e.}$; EJ-299-33 (cyl): ~70 $keV_{e.e.}$; EJ-301: ~60 $keV_{e.e.}$; EJ-309 (10cm × 10 cm × 10 cm and 15 cm × 15 cm × 15 cm): ~90 $keV_{e.e.}$. The light output vs. $E_{e.e.}$ relationship allowed us to determine a dynamic range in terms of proton equivalent energy (*p.e.*) of < 0.5 $MeV_{p.e.}$ – ~7 $MeV_{p.e.}$.

To select out neutron events, the common method is to make selections on a 2-*d* scatter of the aforementioned ratio (the *pulse shape* parameter) vs. the pulse height (energy). Displaying data in this manner (Fig. 6) show two distinct bands of events corresponding to γ rays (pulse shape centroid ~60 ch.) and fast neutrons (pulse shape centroid ~110 ch.). Background and 478 keV γ rays (from the ^{7}Li(*p*,*n*)^{7}Be reaction) are filtered out by event selections (piecewise cuts in Fig. 6). The *pulse shape* parameter was tuned by optimizing the PSD figure of merit (M) using a ^{252}Cf n/γ-ray source, where M is the ratio of the distance between the centroids of the γ-ray and neutron distributions and the sum of the full widths at half maximum (FWHM) of each distribution. Typical

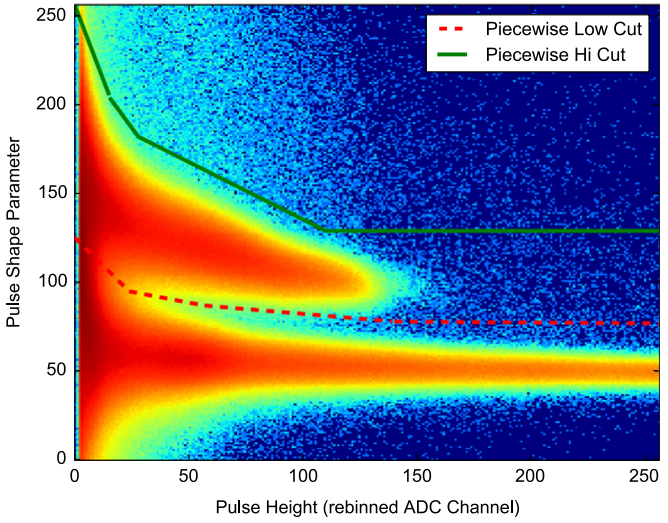

Fig. 6. 2-*d* scatter plot of the pulse shape parameter vs. pulse height (event selections are shown by the piecewise curves).

values of M ranged from 0.5 to 2, dependent on energy and detector type. The spectra of the PSD-selected neutron events for each energy are shown in Fig. 7 for the 10 cm × 10 cm × 10 cm EJ-299-33 cube. Spectra are shown in terms of relative light output based on a measure of the total integrated charge. Data at each energy were acquired for equivalent run times; however, due to variations in the beam current from the accelerator, the counts on the ordinate were scaled accordingly.

To achieve Gaussian statistics ($\sigma \sim \sqrt{n}$) in the neutron-PSD selected band of events and to avoid pulse pile up events, it was requested that the accelerator operate such that each detector would count in the range of 10 kHz (all events) over a five-minute increment by varying the beam current. However, the stability of the accelerator output dictated that it operate with higher beam current (in the 3–5 μA range), and thus count rates of 30–100 kHz were often observed. The typical efficiency of the liquid and plastic scintillator is of order 10 s of percent based on the geometric area of the detector used (~60% for the 15 cm × 15 cm × 15 cm EJ-309 cube) in the fast neutron regime. The acquisition system sampling rate was well equipped to handle the high rate and still able to discriminate incident stimuli based on pulse shape. For data sets

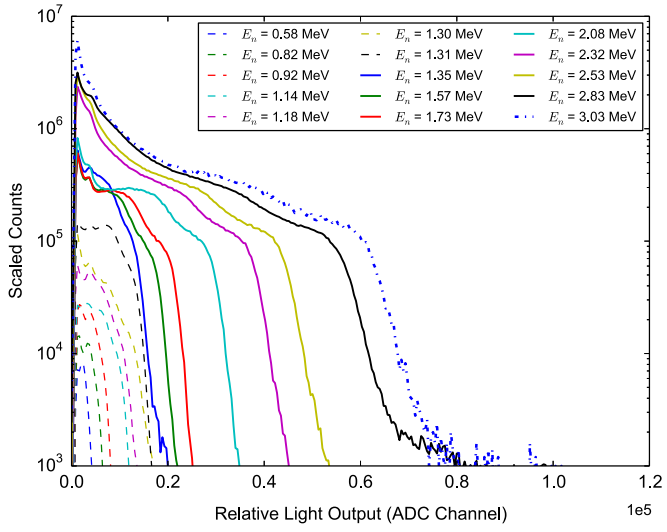

Fig. 7. Neutron energy spectra obtained from the 10 cm × 10 cm × 10 cm cube of EJ-299-33 plastic scintillation detector.

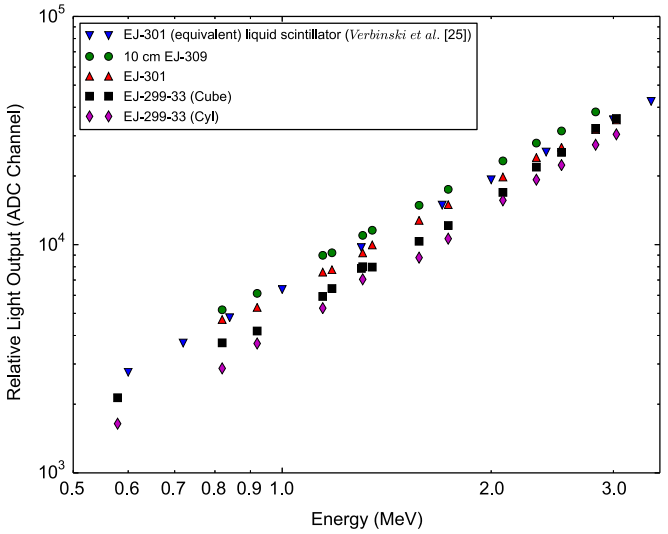

Fig. 8. Response functions for PSD-capable plastic (EJ-299-33) and liquid (EJ-301 and EJ-309) scintillation detectors shown with the previously determined EJ-301 response [25].

where the total event rate exceeded 50 kHz, the number of pile up events and falsely identified PSD events increased. However, given that the edge of the recoil proton spectrum was the main interest for this work and was clearly identified in the analysis procedure, the number of piled up events were acceptable because the main n/γ bands were cleanly separated.

4.2. Analysis

The main focus of the characterization was to test the response of the EJ-299-33 light output vs. recoil proton energy. Based on the spectra shown (Fig. 7), to compare our results with the widely accepted non-linear recoil proton light output vs. energy curves, we follow the method outlined by *Verbinski* et al. [25] where the half height of the abrupt edge near the maximum pulse height corresponds to the maximum hydrogen recoil energy (*n-p* scatter). The enhancement (bump) prior to the edge in each curve in Fig. 7 is the result of neutrons produced from the first excited state of ^{7}Be, which serves as an additional data calibration point. The first excited state sits on the lower energy continuum of down-scattered and background neutrons, leading to the observed broadening.

Spectra from each detector were used to construct a curve of the recoil proton light output vs. energy (response function). To correct for differing gain settings, the curves from each detector and the data from *Verbinski* et al. were normalized to the Compton edge of ^{60}Co as measured by the 12.7-cm diameter EJ-301 cylinder. (The EJ-301 equivalent scintillator was used in the original work of *Verbinski* et al.). Shown in Fig. 8 are the results of the normalized *Verbinski* et al. response, the 10 cm × 10 cm × 10 cm EJ-309 cube, and the EJ-299-33 (cylinder and cube) data in comparison with the 12.7-cm diameter EJ-301 cylinder data. In terms of the general shape of the response, there is good agreement between the data from the 12.7-cm diameter EJ-301 cylinder and *Verbinski* et al., as expected; the 10 cm × 10 cm × 10 cm EJ-309 cube demonstrates a higher light output. The shape of the function for EJ-301 and EJ-299-33 are similar, albeit with EJ-299-33 yielding a lower light output.

For a more quantitative measure of the maximum recoil proton energy and associated error, the spectra accumulated from each detector were fit using the *curve fit* procedure in ScientificPython (SciPy) [26]. The functional form used for the fitting procedure was the complementary error function, *erfc*(*x*) (= 1– *erf*(x), where *erf*(*x*) is the standard error function [27]) on an exponentially decaying background. The user input curve parameters define a fit region from a point prior to the rollover in the spectrum to a point that precedes the high-energy background continuum; the region associated with neutrons arising from the first excited state were fit in the same manner. A background region extending past the endpoint of beam-related neutrons is also defined. The output from the fitting procedure is the centroid of the *erfc*(*x*) and the associated FWHM.

Along with the γ-ray calibration data, the fit results allow us to obtain a relationship for the $E_{e.e.}$ vs. $E_{p.e.}$ The value for the proton recoil centroids were input to the γ-ray calibration curves, defining $E_{e.e.}$; $E_{p.e.}$ is the recoil proton energy imparted by the accelerator-produced neutrons. This relationship is shown in Fig. 9 for the 12.7-cm diameter EJ-301cylinder and the associated FWHM error bars at each energy. These data are shown in comparison with *Verbinski* et al. – the functional form of one of the standard response curves quoted for EJ-301/NE-213 scintillator. The EJ-301 data acquired at the UML facility is in agreement to within error with *Verbinski* et al. Also shown in Fig. 9 are the common light

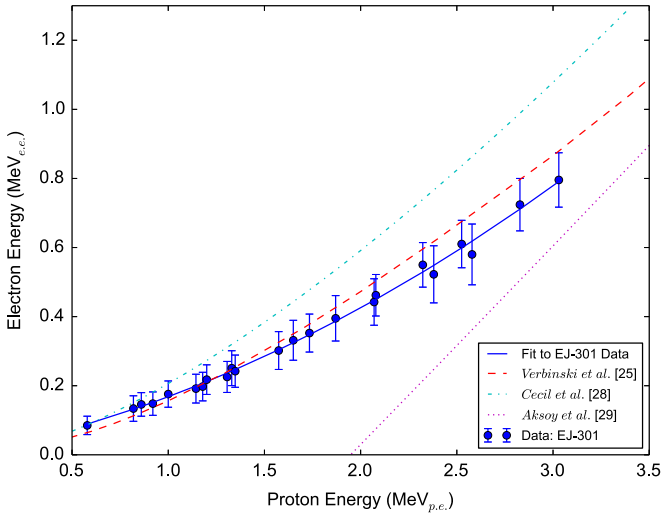

Fig. 9. The relationship between the electron equivalent energy ($E_{e.e.}$) vs. the proton equivalent energy ($E_{p.e.}$) for the data set obtained with the EJ-301. The data (with error bars) are shown for comparison with the functional forms of: *Verbinski* et al. [25], *Cecil* et al. [28], and *Aksoy* et al. [29].

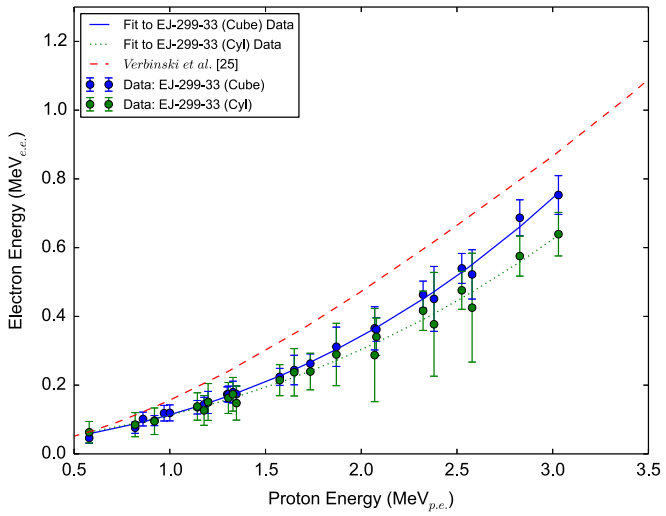

Fig. 10. The relationship between the electron equivalent energy ($E_{e.e.}$) vs. the proton equivalent energy ($E_{p.e.}$) for the data set obtained with the EJ-299-33 (cube and cylinder). The data (with error bars) are shown for comparison with the functional form of *Verbinski* et al. [25].

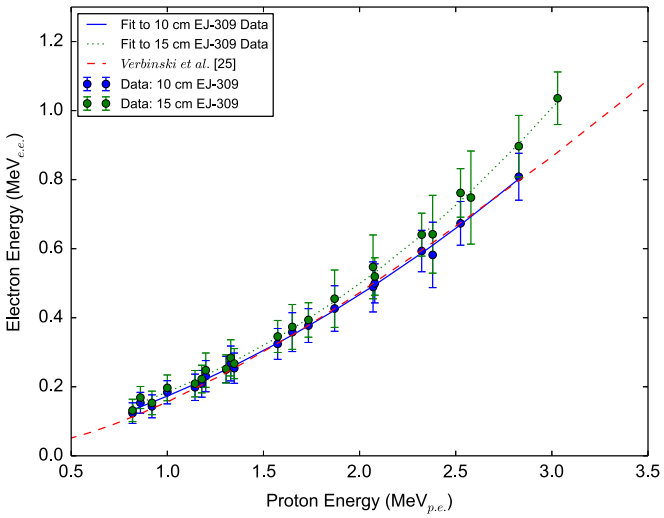

Fig. 11. The relationship between the electron equivalent energy ($E_{e.e.}$) vs. the proton equivalent energy ($E_{p.e.}$) for the data set obtained with the EJ-309 (10 cm × 10 cm × 10 cm and 15 cm × 15 cm × 15 cm cubes). The data (with error bars) are shown for comparison with the functional form of *Verbinski* et al. [25].

response functions for EJ-301 (and its equivalent) provided by the Eljen Technology data sheet [28]·[29]. The results from *Cecil* et al. [28] extend over the range of 1–300 MeV, yielding a higher light output compared to *Verbinski* et al. Conversely, the functional form for $E_{e.e.}$ vs. $E_{p.e.}$ provided by *Aksoy* et al. [29] dramatically underestimates the response. Although it is noted that the *Aksoy* et al. results are valid in the 5–17 MeV energy range, the curve is shown here to demonstrate the inaccuracies of extrapolation to lower energies.

Fig. 10 shows the EJ-299-33 data, displaying that the overall light output is reduced compared to the EJ-301 standard. The curve associated with the EJ-299-33 is fit with the function of the form given by Eq. (2):

$$E_{e.e.} = ae^{(b\ \ln(E_{p.e.}) + c\ \ln\ (E_{p.e.})^2)} \tag{2}$$

where the coefficients were determined to be: $a=0.114$, $b=1.382$, and $c=0.297$ (EJ-299-33 cube); $a=0.112$, $b=1.214$, and $c=0.316$ (EJ-299-33 cylinder).

The response curves for the EJ-309 scintillator are shown in comparison to the standard EJ-301 curve (Fig. 11). One can see that there is excellent agreement for the 10 cm × 10 cm × 10 cm cube; there is also good agreement for the 15 cm × 15 cm × 15 cm cube up to 2.5 MeV$_{p.e.}$, where our measured data diverges from the EJ-301 standard curve, indicating higher light output.

4.3. Monte Carlo simulations

Monte Carlo numerical modeling was carried out using the NRL-developed SWORD (SoftWare for Optimization of Radiation Detection) radiation transport package [30]. The SWORD package provides a graphical CAD system for constructing the simulated scenario with built-in defined detector materials, geometries, and neutron/γ-ray emission spectra. The SWORD framework supports the transport engines of GEANT4 [31] and MCNPX [32].

4.3.1. Neutron beam environment

Using SWORD to simply model the detector response to a monoenergetic neutron beam, results show a single, broadened peak (based on detector energy resolution) centered at the given energy. However, as shown by the measured data in Fig. 12 (*solid curve*), the results show a low-energy continuum preceding the recoil proton edge energy, followed by a background continuum. To properly assess the scenario, a mass model of the representative 15 cm × 15 cm × 15 cm EJ-309 cube was constructed inside the UML facility (volume: 10 m^3, wall material: concrete) situated behind the neutron spectrometer on axis with respect to the target. The full reaction of the Li target undergoing bombardment by 4.7 MeV protons was simulated by isotropic point source emission of 3.03 MeV (from the ground state) and 2.579 MeV (from the first excited state) neutrons from the location of the target with respect to the detector. (The angular dependence of the reaction was not simulated). Events that triggered a hit were then convolved with an energy resolution function of the form: $1/\sqrt{(E)}$, with 32% $\delta E/E$ at 662 keV. The first excited state reaction was scaled by 6% given the relative reaction rate [16]. Summing the simulated events show the low-energy continuum (<2.0 MeV) produced by the down-scattered accelerator neutrons (Fig. 12, *dashed curve*). However, there is a discrepancy between the counts in the low-energy continuum in the sum of the simulated data, compared to the measured data. This discrepancy is also present in the region between the edges corresponding to

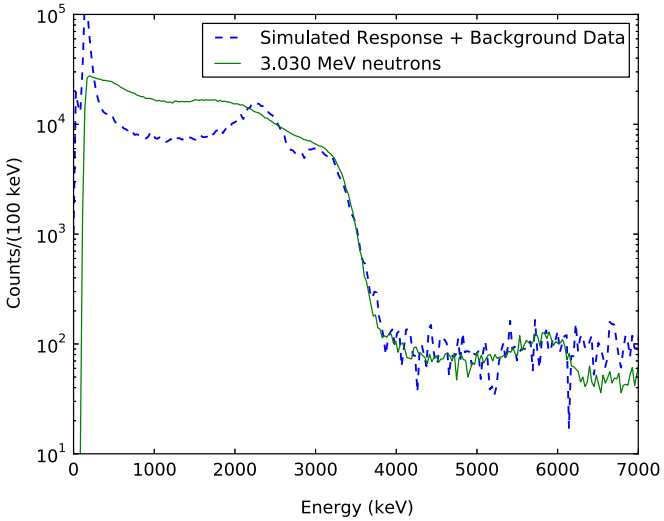

Fig. 12. Comparison of the 3.03 MeV neutron beam measurement (*solid*) and the simulated (with measured background data) response (*dashed*).

neutrons from the ground and first excited state. (To normalize the first excited state neutron events riding on the low-energy continuum, we matched the relative heights of ground state and first excited state in the observed data. The first excited state reaction was increased by a factor of 2.5 relative to the ground state). The sum of the simulated data is lower by a factor of ~2–4. This result could be attributed to piled-up events contaminating the neutron-PSD selected events in the measured data, leading to the increase in counts. The likelihood for the false identification of neutron-PSD selected events, especially at lower energy (pulse height), increased due to the high flux encountered during the experiment.

To assist in fully understanding the resulting distribution, we must consider other competing reactions that can occur within the organic scintillator, such as elastic scattering between neutrons and constituent carbon nuclei (*n-C* scatters). Experimentally there is no reliable way to account or correct for these events in the fast neutron energy range. For *n-C* scatters, the neutron can transfer up to 28% of its incident energy to the recoil carbon, whereas in the case of the *n-p* scatter the neutron can deposit up to 100% of its incident energy to the recoil proton [33]. On average, a *n-C* scatter occurring prior to a *n-p* scatter results in a 14% lower energy deposit to the recoil proton (assuming the neutron deposits its full energy in the reaction), which could additionally contribute to the low-energy continuum. For a *n-C* scatter occurring after the *n-p* scatter, recoil carbon produces an undetectable amount of scintillation light in the few MeV neutron range and thus would not contribute to the overall measured pulse height. Moreover, the cross section for elastic *n-p* scattering in the few MeV range is greater than that for elastic *n-C* scattering by a factor of ~2, aside from the resonance reactions in the 3–6 MeV range. The inelastic *n-C* scattering cross section, which has a comparable cross section to the elastic *n-C* reaction above 7 MeV, was not considered in this work.

4.3.2. Background data + neutron beam simulation

For the background, a five minute data set at the UML facility did not show what was observed above 4 MeV in Fig. 12 (*solid curve*). The high-energy background component is thus a combination of contaminated events within the neutron PSD selection with some contribution from high-energy background neutrons. A data set with either: the beam stop in or with the detector situated elsewhere (not in the beam path) with the beam on could have been beneficial in having a better understanding of the accelerator background environment. A long (multi-hour) surrogate background set was taken in the laboratory at NRL to build up the statistics of the high-energy component. The accelerator beam-related events that produce the high-energy, flat continuum are mimicked in the long background data set above 4 MeV. The final product shown by the *dashed curve* in Fig. 12 are the simulated neutron events from the ground state and normalized first excited state from the Li reaction summed with the energy-calibrated, neutron-PSD selected background. (The background data set was normalized to match the observed high-energy continuum; the effects of normalization are observed in the low-energy tail occurring ~100 keV). The curves in Fig. 12 show a qualitative comparison of the simulated + measured background data (*dashed*) with the accelerator-produced 3.03 MeV neutron data set (*solid*). Overall, there is good, relative agreement between the data sets.

5. Discussion and conclusions

The work presented demonstrates a thorough analysis of the light output response function for the novel PSD-capable plastic scintillator, EJ-299-33. Liquid scintillators were tested along with the EJ-299-33, serving as the control given that the liquid response is well documented and understood. The experiment to characterize the detectors was conducted with quasi-monoenergetic neutrons as measured by a flash ADC data acquisition system performing digital PSD with a fast sample rate. The neutron energy, based on the location in the recoil proton spectrum, was determined qualitatively (observing the half height) and quantitatively (curve fitting). Results show that the behavior of the EJ-301 liquid scintillator is in good agreement with the canonical work done previously (Fig. 9). The EJ-309 liquid scintillator is said to have slightly less light output than the EJ-301 [19], yet Fig. 11 demonstrates that the light output is comparable ($10\ \text{cm} \times 10\ \text{cm} \times 10\ \text{cm}$ cube) or higher by ~30–40% for $> 2\ \text{MeV}_{p.e.}$ ($15\ \text{cm} \times 15\ \text{cm} \times 15\ \text{cm}$ cube). Table 3 shows that the difference in light output of a few percent between the EJ-301 and EJ-309 [3,18,19]. A potential explanation for our results could be due to the inherent manufacturing of the detector (slight impurities in the scintillator, reflective inner surfaces of the detector, PMT differences, detector geometry, etc).

The response functions obtained for the two different geometry EJ-299-33 plastic scintillation detectors tested were in agreement to within error for the energy range between 0.5–3.0 $\text{MeV}_{p.e.}$. For energies $< 2.0\ \text{MeV}_{p.e.}$ the light output from each detector is equivalent; above $2.0\ \text{MeV}_{p.e.}$ the EJ-299-33 cube shows a higher light output by up to 20%. The two EJ-299-33 detectors were equal in everything except geometry; as a result, differences in the light output due to the manufacturing process, and inherently due to the geometry, cannot be ruled out.

The difference in light output between the liquid and plastic scintillation detectors is shown in Table 3. Our results for the comparison between EJ-299-33 and EJ-301 are shown graphically by the data points in Figs. 8 and 10. By comparing the EJ-301 liquid scintillator with the EJ-299-33 plastics, we observe a reduction in light output by ~40% in the cube and cylinder at low energies ($< 1.0\ \text{MeV}_{p.e.}$); for increasing energy ($> 2.0\ \text{MeV}_{p.e.}$) the light output of the EJ-301 and the cube are comparable (within 5%) while the cylinder shows a reduction by ~20%. For the EJ-309 liquid scintillator, comparing the $10\ \text{cm} \times 10\ \text{cm} \times 10\ \text{cm}$ liquid and the EJ-299-33 cube, we observe 40% less light from the cube below $1.0\ \text{MeV}_{p.e.}$ and improving to ~20% reduction for energies $> 2.0\ \text{MeV}_{p.e.}$. For the EJ-299-33 cylinder, we observe a reduction of ~32% in light compared to the liquid across the energy range sampled. Lastly, comparing the $15\ \text{cm} \times 15\ \text{cm} \times 15\ \text{cm}$ EJ-309 and the EJ-299-33 plastics, we find a ~40% reduction in light output for the cylinder and a reduction ranging from ~40% ($< 1.0\ \text{MeV}_{p.e.}$) to ~25% ($> 2.0\ \text{MeV}_{p.e.}$) for the cube.

Acknowledgments

This work was sponsored by the Office of Naval Research (ONR). The authors would like to thank the staff for their assistance at the University of Massachusetts Lowell, namely, Partha Chowdhury, Christopher Lister, Gregg Parker, Nathan D'Olympia, and Emily Jackson.

References

[1] F.D. Brooks, et al., IRE. T. Nucl. Sci. 7 (2-3) (1960) 35.
[2] N. Zaitseva, et al., Nuclear instruments and methods in physics research section a: accelerators, spectrometers, Detectors Assoc. Equipment 668 (2012) 88.
[3] Eljen Technology, EJ-299-33. ⟨http://www.eljentechnology.com/index.php/products/plastic-scintillators/114-ej-299-33⟩.
[4] A. Zimbal, et al., Proceedings of Science – International Workshop on Fast Neutron Detectors, University of Cape Town, South Africa (2006) (3–6 April).
[5] N. Mascarenhas, et al., IEEE NSS/MIC Conference Record 1 (2006) 185.
[6] R.S. Woolf, et al., Proceedings of SPIE – Solar Physics and Space Weather Instrumentation III 7438 (2009) 19.

[7] S.A. Pozzi, et al., Nucl. Instrum. Meth. Phys. Res. A. 723 (C) (2013) 19.
[8] S. Nyibule, et al., Nucl. Instrum. Meth. Phys. Res. A. 728 (C) (2013) 36.
[9] D. Cester, et al., Nucl. Instrum. Meth. Phys. Res. A. 735 (C) (2014) 202.
[10] C.C. Lawrence, et al., Nucl. Instrum. Meth. Phys. Res. A. 759 (2014) 16.
[11] J.A. Jungerman, F.P. Brady, Nucl. Instrum. Meth. 89 (1970) 167 (1 December).
[12] M.F. Wolff, IEEE Spectrum. 27 (7) (1990) (July).
[13] B.A. Ludewigt, et al., Nuclear Instruments and Methods in Physics Research Section B, Beam Interact. Mater. Atoms 261 (1-2) (2007) 830.
[14] G.H.R. Kegel, Nucl. Instrum. Meth. Phys. Res., B. 40/41 (1989) 1165.
[15] P. Staples, et al., Nucl. Instrum. Meth. Phys. Res. A. 591 (1995) 41.
[16] H. Liskien, A. Paulsen, Atom. Data Nucl. Data Tables 15 (1975) 57.
[17] ET Enterprises, Photomultipliers from ET Enterprises Ltd, ETL 9265KB. ⟨http://www.et-enterprises.com/photomultipliers⟩.
[18] Eljen Technology, EJ-301. ⟨http://www.eljentechnology.com/index.php/products/liquid-scintillators/71-ej-301⟩.
[19] Eljen Technology, EJ-309. ⟨http://www.eljentechnology.com/index.php/products/liquid-scintillators/73-ej-309⟩.
[20] ISEG Germany, EDS. ⟨http://www.iseg-hv.com/en/products/product-details/product/20/⟩.
[21] CAEN Electronic Instrumentation, CAEN SY2527 Universal Multichannel Power Supply System. ⟨http://www.caen.it/csite/CaenProd.jsp?parent=20&idmod=123⟩.
[22] Struck Innovative Systeme, SIS3316-250-14 16 channel 250 MSPS 14-bit. ⟨http://www.struck.de/sis33166.html⟩.
[23] F.D. Brooks, Nucl. Instrum. Meth. 4 (1959) 151.
[24] H.H. Knox, T.G. Miller, Nucl. Instrum. Meth. 101 (3) (1972) 519.
[25] V.V. Verbinski, et al., Nucl. Instrum. Meth. 65 (1968) 8.
[26] Scientific Python, SciPy.org. ⟨http://www.scipy.org/docs.html⟩.
[27] J. Matthews,, R.L. Walker, Mathematical Methods of Physics, 2nd, ed., Addison-Wesley Publishing Co., (1970) 77.
[28] R.A. Cecil, et al., Nucl. Instrum. Meth. 161 (1979) 439.
[29] A. Aksoy, et al., Nucl. Instrum. Meth. Phys. Res. A. 337 (s 2-3) (1994) 486.
[30] C. Gwon, et al., IEEE NSS/MIC Conference Record 2 (2007) 1130.
[31] S. Agostinelli, et al., Nucl. Instrum. Meth. Phys. Res. A. 506 (3) (2003) 250.
[32] Monte Carlo N-Particle (MCNP), MCNPX-5 Monte Carlo Team, LA-UR-03-1987, Los Alamos National Laboratory, Los Alamos, NM.
[33] G.F. Knoll, Radiation Detection and Measurement, 3rd, ed., Wiley, New York (2000) 553.